PAPER

Check for updates

Broad-band sensitized visible up-conversion in $Y_2Mg_3Ge_3O_{12}$:Ni^{2+},Er^{3+},Nb^{5+} phosphors†

Weiqi Yang, [ID] Siguo Xiao, [ID] * Xiaoliang Yang and Yaoxiang Zhao

Ni^{2+}, Er^{3+}, Nb^{5+} tri-doped $Y_2Mg_3Ge_3O_{12}$ phosphors have been fabricated using a conventional solid-phase reaction method. Near infrared light in the wavelength range of 900–1700 nm can be up-converted by the phosphors into visible emissions peaking at 532 nm, 555 nm and 675 nm of Er^{3+}, performed by the $Ni^{2+} \rightarrow Er^{3+}$ and $Er^{3+} \rightarrow Er^{3+}$ energy transfers. The introduction of Nb^{5+} ions can adjust the local environment of Ni^{2+} and Er^{3+} ions and thus effectively reduces their nonradiative transition probability, which largely enhances the intensity of up-conversion emission. The effects of Ni^{2+} and Er^{3+} concentration together with the excitation power on the fluorescence properties have been investigated. The $Y_2Mg_3Ge_3O_{12}$:$0.015Ni^{2+}$,$0.13Er^{3+}$,$0.06Nb^{5+}$ phosphor manifests the optimal UC emission effectiveness in this work, in which the energy transfer sensitization from $Ni^{2+} \rightarrow Er^{3+}$ induced by quadrupole-quadrupole interaction is as high as 92.1%. The developed broadband near-infrared excitable up-conversion materials are promising for extensive photonic applications, including c-Si solar cells and infrared detectors.

1. Introduction

As the research on rare earth (RE) ion doped up-conversion (UC) materials has continued, many UC materials with different characteristics have been created. They have attracted a lot of attention owing to their excellent properties and special characteristics for multi-color displays, optical processing sensors, solid-state lasers, optical data storage, solar cells, infrared detection, photodynamic therapy, bioimaging and other fields.[1–8] With the increasing emphasis on green energy, especially since solar radiation is a readily available renewable energy source, the high-efficiency utilization of solar radiation has received a lot of attention in the field of photovoltaics. Because of the Shockley–Queisser (S–Q) limit, however, the efficiencies of the current solar cells are still not satisfactory. To illustrate, the typical single-junction crystalline silicon solar cell currently has a peak conversion efficiency of only 33% for solar energy. The crystalline silicon solar cell has an absorption threshold of about 1127 nm, which is wasteful of solar radiation energy in the near-infrared (NIR) region.[9–14] Fortunately, the UC process that can convert the near-infrared wavelength to the usable wavelength of solar cells seems to be an effective way to solve this problem.[15–17]

In the case of UC materials, Yb^{3+} ions can be doped widely as a sensitizer ion to improve the optical pump efficiency of

School of Physics and Optoelectronics, Xiangtan University, Hunan 411105, China.
E-mail: xiaosiguo@xtu.edu.cn

† Electronic supplementary information (ESI) available. See DOI: https://doi.org/10.1039/d2ma00519k

activator ions including Er^{3+}, Tm^{3+} and Ho^{3+}. For example, the UC emission of 500–700 nm is obtained for β-$NaYF_4$:$17\%Yb^{3+}$,$3\%Er^{3+}$ at 980 nm excitation, and its UC quantum efficiency (QE) is 10.5% at an excitation power density of 30 W cm^{-2}. Other high-efficiency UC materials including BaF_2:$3\%Yb^{3+}$,$2\%Er^{3+}$ (QE = 10.0% at excitation power density 490 W cm^{-2}), La_2O_2S:$9\%Yb^{3+}$,$1\%Er^{3+}$ (QE = 5.8% at excitation power density of 13 W cm^{-2}), and BaY_2ZnO_5:$7\%Yb^{3+}$,$3\%Er^{3+}$ (QE = 5% at excitation power density of 2.2 W cm^{-2}) have also been reported.[18–21] This is attributed to the large absorption cross section of Yb^{3+} at around 980 nm and the efficient energy transfer (ET) from Yb^{3+} to the activator ion.[22–24] Regretfully, the narrow absorption bandwidth of Yb^{3+} due to its parity forbidden 4f–4f transition, limits the practical application of the Yb^{3+} sensitized UC phosphor in some fields such as solar cell efficiency enhancement and infrared detection. Thus, it is expected to break through the bottleneck of traditional UC phosphor to find new sensitizers that can absorb infrared light in a wide wavelength and transfer the absorbed energy to the activator ions such as Er^{3+}, Tm^{3+} and Ho^{3+}. It was reported recently that dye-sensitized core/shell nanocrystals can capture photons over a broad range of wavelengths (720–1000 nm) and significantly enhance the overall UC efficiency.[25] On the other hand, as transition metal ions (Ni^{2+}, Cr^{3+}, *etc.*) have been widely studied, they have demonstrated satisfactory wavelength-tunable fluorescence properties due to their customary $3d^n$ electron structure and sensitivity to the surrounding crystal field environment.[26–28] As a consequence of their properties of a wider absorption band than that of Yb^{3+}, some transition metal ions are also used as sensitizers in some

© 2022 The Author(s). Published by the Royal Society of Chemistry

UC phosphors. For example, in the Cr^{3+}–Er^{3+} double-doped $La_3Ga_5GeO_{14}$, UC emission of Er^{3+} in the 510–570 nm region under 620 nm excitation sensitized by the Cr^{3+} has been observed.[29,30] Similarly, UC emission of Er^{3+}/Tm^{3+} sensitized by Ni^{2+} has also been realized in phosphors such as (Mg, Ca, Sr, Ba)TiO_3:Ni^{2+},Er^{3+}, $MgGa_2O_4$:Ni^{2+},Er^{3+}, $LiGa_5O_8$:Ni^{2+},Tm^{3+}, La(Ga, Sc, In)O_3:Ni^{2+},Er^{3+}, etc.[31–37] Therefore, Ni^{2+} sensitized UC phosphors might be promising materials for up-converting photons in a wide near infrared wavelength region into a higher energy photon due to the broad band absorption of Ni^{2+}.

Phosphors based on $Y_2Mg_3Ge_3O_{12}$ have been reported several times in very recent years, including $Mg_3Y_2Ge_3O_{12}$:Ce^{3+}, $Mg_3Y_2Ge_3O_{12}$:Sm^{3+}, $Mg_3Y_{2-x-y}Ge_3O_{12}$:xTb^{3+},yEu^{3+}, and $Y_2Mg_3Ge_3O_{12}$:Mn^{4+},Li^+, etc.[38–41] $Y_2Mg_3Ge_3O_{12}$ has a garnet structure, and it has three cationic sites with different valence states (+2, +3, +4) that can accommodate the insertion of various RE ions and transition metal ions. This means that the $Y_2Mg_3Ge_3O_{12}$ matrix is possibly a suitable environment for performing the Ni^{2+} sensitized UC of RE ions. In the current study, therefore, Ni^{2+}, Er^{3+}, Nb^{5+} tri-doped $Y_2Mg_3Ge_3O_{12}$ phosphors have been fabricated and broad band NIR light in the wavelength range of 900–1700 nm to visible UC has been used for the first time.

2. Experimental methods

2.1. Materials synthesis

With a conventional high temperature solid-phase reaction method, a range of samples with polycrystalline powder, $Y_2Mg_{3(1-x)}Ge_3O_{12}$:xNi^{2+} (x = 0.005, 0.015, 0.025, 0.035, 0.045 and 0.055), $Y_{2(1-y)}Mg_{3(1-x-z)}Ge_3O_{12}$:$xNi^{2+}$,$yEr^{3+}$,$zNb^{5+}$ (x = 0, 0.001 and 0.015, y = 0, 0.001 and 0.11, z = 0, 0.015, 0.03, 0.045, 0.06 and 0.075), and $Y_{2(1-y)}Mg_{3(1-x-0.06)}Ge_3O_{12}$:$xNi^{2+}$,$yEr^{3+}$,0.06$Nb^{5+}$ (x = 0.005, 0.01, 0.015, 0.02, 0.025, y = 0.11, y = 0.05, 0.07, 0.09, 0.11, 0.13, 0.15, 0.17 and x = 0.015) were prepared. The powders MgO (AR), Y_2O_3 (99.99%), GeO_2 (99.99%), NiO (AR), Er_2O_3 (99.99%) and Nb_2O_5 (AR) were weighed according to the stoichiometric amounts as raw materials. The weighed raw materials were fully ground and mixed in an agate mortar, and the mixtures were subsequently transferred into corundum crucibles. The mixtures were calcined at a temperature of 1500 °C for 7 hours in an electric furnace under an air atmosphere. Eventually, the products were taken out after waiting for natural cooling to room temperature as well as being milled again into powders for further characterization.

2.2. Characterization

In order to identify the purity of the crystalline phase in the sample, X-ray diffraction (XRD) patterns were analyzed which were documented using a Bruker D8 Focus Diffractometer (Instrument Model: PIGAKV Ultima IV Device) utilizing Cu/Kα (λ = 0.1541 nm) radiation over the 2θ scale in the range of 10° to 90° with a scan step of 0.02° and a scan rate of 10° min^{-1}. The absorption spectra of the samples doped with Ni^{2+} and Er^{3+} were analyzed using a Hitachi UH5700 Spectrophotometer (Integrating Sphere) running at a scan step of 1 nm. The UC

emission and Stokes emission spectra were analyzed by using the diode lasers of 455 nm, 980 nm, 1064 nm, 1342 nm, and 1550 nm as well as a 150 watt xenon lamp as the excitation sources on a monochromator (Zolix Instrument, Omni-λ320i) which was equipped with a photomultiplier tube (PMTHS1-R928) and a data acquisition system with a scan step of 1 nm. The sample was placed in a solid sample holder. The powder sample was kept in a small hollow metal container and the container was filled with the powder. Then, the surface of the powder was made smooth by pressing with a glass slide in order to make sure all measurements were done on an equal amount of material. Moreover, the sample was placed between the excitation and emission monochromator in such a way that the emitted light signal from the sample was directed at 90° with respect to the incident light. Great care was taken in the setup to assure the material was placed in the exact same measuring position for each measurement. The time decay curves were analyzed using the FLS980 (Edinburgh) spectrometer operating at 380 nm, 455 nm and 1064 nm excitation. All the measurements were performed at room temperature.

3. Results and discussion

$Y_2Mg_3Ge_3O_{12}$ has a garnet structure with the space group $Ia\bar{3}d$ (230). Its cations occupy a total of three different sites. In detail, Y^{3+} and one third of Mg^{2+} occupy the center of the dodecahedra. The remaining two-thirds of Mg^{2+} occupy the sites of the octahedral centers and Ge^{4+} is located in the tetrahedral sites. Fig. 1 shows the enlargement of the crystal structure of $Y_2Mg_3Ge_3O_{12}$. Table 1 shows the effective ionic radius of the different ions. Due to the similar effective ionic radius and the same chemical valences, the doped Ni^{2+} and Er^{3+} can well replace the lattice sites of Mg^{2+} and Y^{3+} in the $Y_2Mg_3Ge_3O_{12}$ matrix, respectively. It is well-known that Ni^{2+} usually exhibits the habit of preferentially occupying the octahedral site.[27] After Ni^{2+} is doped into the $Y_2Mg_3Ge_3O_{12}$ matrix, therefore, it is going to occupy the octahedral Mg^{2+} site. It is found that Nb^{5+} ions can replace the ions with valence +1, +2 and +3.[42,43] Therefore, Nb^{5+} might occupy both Mg^{2+} and Y^{3+} sites. When a Nb^{5+} ion occupies a Mg^{2+} site, a Y^{3+} ion vacancy will be created. When a Nb^{5+} ion occupies a Y^{3+} site, a Mg^{2+} ion vacancy will be created. Thus, the vacancies induced by the doped Nb^{5+} ions will cause distortion
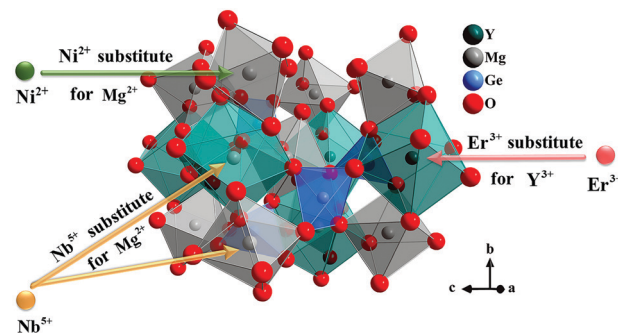

Fig. 1 Enlargement of the crystal structure of $Y_2Mg_3Ge_3O_{12}$.

Table 1 Effective ionic radius at the different coordination numbers (CN)

| Ion	CN = 8				CN = 6			CN = 4
	Y^{3+}	Mg^{2+}	Nb^{5+}	Er^{3+}	Mg^{2+}	Ni^{2+}	Nb^{5+}	Ge^{4+}
Ionic radius (Å)	1.019	0.89	0.74	1.004	0.72	0.69	0.64	0.39

of the lattice host, which might reduce the local symmetry of Ni^{2+} and Er^{3+} luminescence centers and is beneficial to improve their luminescent properties. The XRD patterns of some prepared samples are given in Fig. 2, including the $Y_2Mg_3Ge_3O_{12}$ host, Ni^{2+}, Er^{3+} and Nb^{5+} mono-doped $Y_2Mg_3Ge_3O_{12}$, Ni^{2+}, Er^{3+} double-doped, Er^{3+}, Nb^{5+} double-doped and Ni^{2+}, Nb^{5+} double-doped $Y_2Mg_3Ge_3O_{12}$ and Ni^{2+}, Er^{3+}, Nb^{5+} tri-doped $Y_2Mg_3Ge_3O_{12}$. Most of the diffraction peaks for these samples could be in good agreement with the standard card data of $Y_2Mg_3Ge_3O_{12}$ (PDF#89-6603). By careful comparison, however, two impurity peaks are found at two thetas of 28.6 and 30.2 degrees in the sample doped with Nb^{5+}, which likely belong to $YNbO_4$ (PDF#72-2077). Fortunately, the content of the impurity is relatively slight and the XRD pattern of the main phase $Y_2Mg_3Ge_3O_{12}$ has not been interfered with, meaning that the impurity has no effect on the crystal structure of the phosphors.

The absorption spectra of $0.015Ni^{2+}$ mono-doped and $0.11Er^{3+}$ mono-doped $Y_2Mg_3Ge_3O_{12}$ powders in the range of 870–1700 nm are given in Fig. 3. For the Ni^{2+} mono-doped sample, a broad and strong absorption band in the range of 900–1600 nm is observed, which is due to the spin-allowed d–d transition from $^3A_2(^3F)$ to $^3T_2(^3F)$ of Ni^{2+} substituting the octahedral Mg^{2+}. The Er^{3+} mono-doped sample has two absorbing bands peaking at 966 nm and 1500 nm, respectively. They are ascribed to the f–f transitions of Er^{3+} ions from the ground state ($^4I_{15/2}$) to the $^4I_{11/2}$ and $^4I_{13/2}$ excited states, respectively. The absorption of Er^{3+} and Ni^{2+} ions together forms a wide absorption band covering from 900 nm to 1700 nm. Fig. 4 shows the NIR emission spectra of $Y_2Mg_3Ge_3O_{12}$:xNi^{2+} (x = 0.005, 0.015, 0.025, 0.035, 0.045 and 0.055) samples under excitation of 1064 nm. The excitation light of 1064 nm is located exactly in the absorption band of Ni^{2+}: $^3A_2 \rightarrow {}^3T_2$. The Ni^{2+} mono-doped sample exhibits
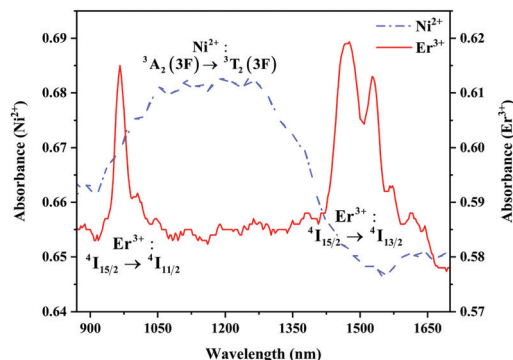
Fig. 3 Absorption spectra of $0.015Ni^{2+}$ mono-doped and $0.11Er^{3+}$ mono-doped $Y_2Mg_3Ge_3O_{12}$.

broadband NIR emission within the 1100 nm to 1700 nm range due to its $^3T_2 \rightarrow {}^3A_2$ transition. The NIR emission intensity reaches the maximum at the concentration of Ni^{2+} up to 0.015 and then begins to decrease at higher Ni^{2+} concentration due to the concentration quenching effect.

The UC emission spectra of Ni^{2+} mono-doped, Er^{3+} mono-doped, and Ni^{2+}, Er^{3+} double-doped $Y_2Mg_3Ge_3O_{12}$ samples in the 500–700 nm range under 980 nm and 1064 nm excitation are shown in Fig. 5. The UC emission of the Er^{3+} mono-doped and Ni^{2+}, Er^{3+} double-doped samples at 980 nm excitation is clearly observed in Fig. 5a, which originates from the Er^{3+}: $^4F_{9/2} \rightarrow {}^4I_{15/2}$ transition (675 nm), Er^{3+}: $^4S_{3/2} \rightarrow {}^4I_{15/2}$ transition (555 nm) and Er^{3+}: $^2H_{11/2} \rightarrow {}^4I_{15/2}$ transition (532 nm), respectively. On the other hand, although the 980 nm and 1064 nm light both fall into the Ni^{2+}: $^3A_2 \rightarrow {}^3T_2$ absorption band, the UC emission is not observed in the Ni^{2+} mono-doped sample either with the excitation of 980 nm or 1064 nm. This implies that the Er^{3+} ions can conduct the UC process with the excitation at 980 nm, while the Ni^{2+} ion cannot perform the UC by itself. Not surprisingly, the Er^{3+} mono-doped sample also does not give UC emission under 1064 nm excitation since the incident 1064 nm phonon cannot be absorbed by Er^{3+} ions (in Fig. 5b). Of interest, relatively obvious UC emission at 675 nm and 555 nm originating from the Er^{3+}: $^4F_{9/2} \rightarrow {}^4I_{15/2}$ and $^4S_{3/2} \rightarrow {}^4I_{15/2}$ transitions and a weak UC
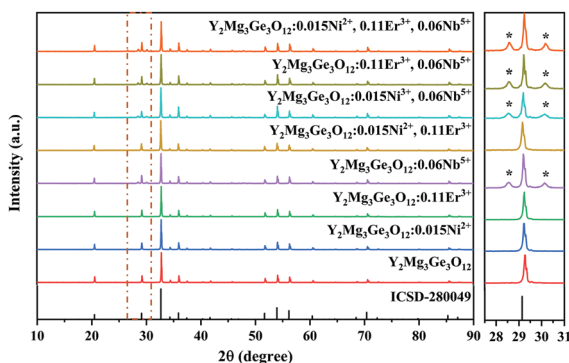
Fig. 2 XRD patterns of the $Y_2Mg_3Ge_3O_{12}$ host, Ni^{2+}, Er^{3+} and Nb^{5+} mono-doped $Y_2Mg_3Ge_3O_{12}$, Ni^{2+}, Er^{3+} double-doped, Er^{3+}, Nb^{5+} double-doped and Ni^{2+}, Nb^{5+} double-doped $Y_2Mg_3Ge_3O_{12}$ and Ni^{2+}, Er^{3+}, Nb^{5+} tri-doped $Y_2Mg_3Ge_3O_{12}$.
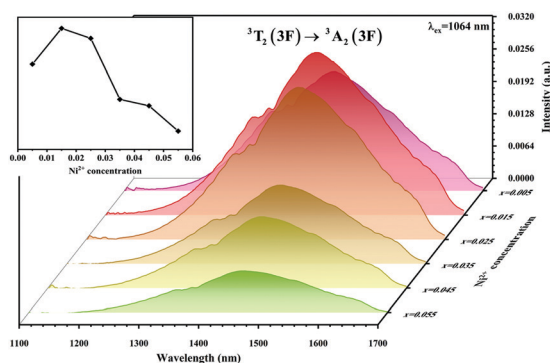
Fig. 4 NIR emission spectra of $Y_2Mg_3Ge_3O_{12}$: xNi^{2+} (x = 0.005, 0.015, 0.025, 0.035, 0.045 and 0.055) samples under 1064 nm excitation. The inset shows the effect of Ni^{2+} concentrations on the NIR emission intensity.
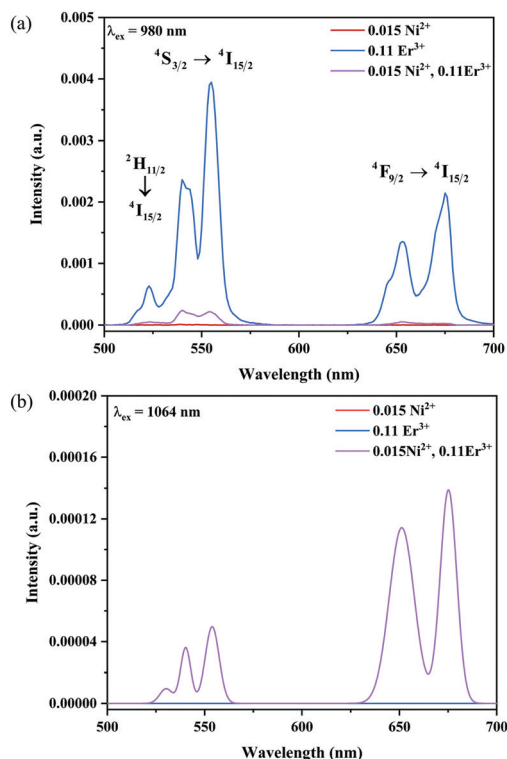
Fig. 5 UC emission spectra of the Ni^{2+} mono-doped, Er^{3+} mono-doped and Ni^{2+}, Er^{3+} double-doped $Y_2Mg_3Ge_3O_{12}$ samples with excitation at 980 nm and 1064 nm.

Fig. 6 1064 nm excited UC emission spectra for $Y_2Mg_3Ge_3O_{12}$:0.015-Ni^{2+},0.11Er^{3+},zNb^{5+} (z = 0.015, 0.03, 0.045, 0.06 and 0.075) (a), and 1064 nm excited UC spectral comparison for the Ni^{2+}, Er^{3+} double-doped and Ni^{2+}, Er^{3+} and Nb^{5+} tri-doped samples (b). The inset shows the variation of green and red emission intensities with the Nb^{5+} ion concentrations, respectively.

emission at 532 nm originating from the Er^{3+}: $^2H_{11/2} \rightarrow {}^4I_{15/2}$ transition are detected for the Ni^{2+}, Er^{3+} double-doped sample under the excitation of 1064 nm. This illustrates that the incident 1064 nm photon is absorbed by the Ni^{2+} ion and then the Er^{3+} is sensitized by the energy transfer from the Ni^{2+} ion to the Er^{3+} ion, resulting in the emissions at 675 nm, 555 nm and 532 nm. The different UC properties of the Ni^{2+}, Er^{3+} mono-doped and Ni^{2+}, Er^{3+} double-doped $Y_2Mg_3Ge_3O_{12}$ with the excitation of 1064 nm and 980 nm prove the occurrence of the $Ni^{2+} \rightarrow Er^{3+}$ energy transfer sensitization. It should be noted that no UC emission has been observed in the Ni^{2+} doped $YNbO_4$, Er^{3+} doped $YNbO_4$ and Ni^{2+}, Er^{3+} co-doped $YNbO_4$ samples under 1064 nm excitation (as shown in Fig. S1, ESI†), which implies that the UC emission of Er^{3+} sensitized by Ni^{2+} is only performed in the $Y_2Mg_3Ge_3O_{12}$ host.

Fig. 6 and 7 show the effects of the samples on the luminescence intensity with the introduction of Nb^{5+} ions. In Fig. 6, it can be observed that the UC luminescence intensity of the Ni^{2+}, Er^{3+} and Nb^{5+} tri-doped samples is significantly enhanced compared with that of the Ni^{2+}, Er^{3+} double-doped sample with the excitation at 1064 nm. When the Nb^{5+} concentration is 0.06, the total UC emission intensity is increased by 22 times. Fig. 7 also shows the effect of Nb^{5+} on the emission of the Ni^{2+} mono-doped and Er^{3+} mono-doped samples, respectively. The Ni^{2+}: $^3T_2 \rightarrow {}^3A_2$ emission intensity of the 0.015Ni^{2+}, 0.06Nb^{5+} double-doped sample is enhanced by 1.5 times compared with that of the 0.015Ni^{2+} mono-doped sample under 1064 nm excitation. Meanwhile, the UC emission intensity of the 0.11Er^{3+}, 0.06Nb^{5+} double-doped sample is significantly
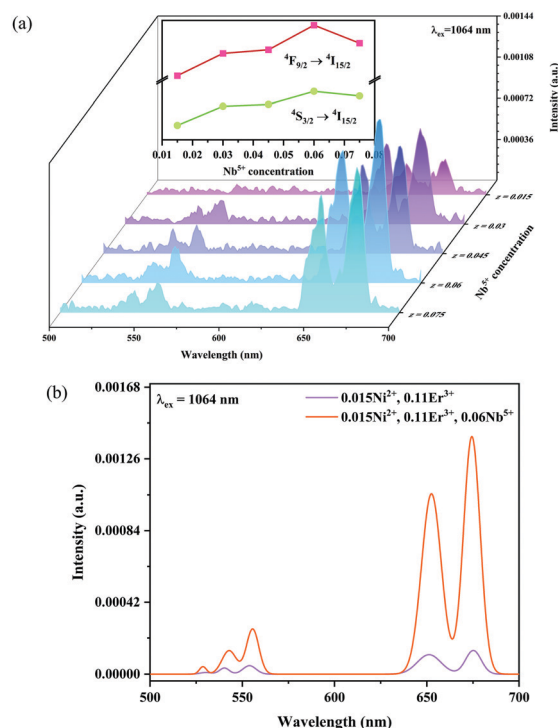
enhanced in the range of 500–700 nm compared with that of the 0.11Er^{3+} mono-doped sample under 980 nm excitation. It is found that the intensities of the UC emission bands at 532 nm, 555 nm and 675 nm for the 0.11Er^{3+}, 0.06Nb^{5+} double-doped sample are enhanced by 11.7, 4.3 and 1.8 times as compared with that of the 0.11Er^{3+} mono-doped sample, respectively. In a word, the introduction of Nb^{5+} ions can improve the luminescence properties of Ni^{2+} and Er^{3+} simultaneously.

Fig. 8a shows the percentage of the UC intensity of the $^2H_{11/2} \rightarrow {}^4I_{15/2}$, $^4S_{3/2} \rightarrow {}^4I_{15/2}$ and $^4F_{9/2} \rightarrow {}^4I_{15/2}$ emissions in the total UC emission intensity for the 0.11Er^{3+} mono-doped and 0.11Er^{3+}, 0.06Nb^{5+} double-doped samples with the excitation at 980 nm, respectively. It is found that the $^2H_{11/2} \rightarrow {}^4I_{15/2}$ and $^4S_{3/2} \rightarrow {}^4I_{15/2}$ emission intensity is largely enhanced as compared that of the $^4F_{9/2} \rightarrow {}^4I_{15/2}$ emission intensity with the introduction of Nb^{5+}. Surprisingly, when Nb^{5+} is introduced, the percentage of $^2H_{11/2} \rightarrow {}^4I_{15/2}$ and $^4S_{3/2} \rightarrow {}^4I_{15/2}$ UC emissions of the Er^{3+} increases by 14% and 3%, respectively, while the percentage of the $^4F_{9/2} \rightarrow {}^4I_{15/2}$ UC emission intensity decreases by 17%. This indicates that the introduction of Nb^{5+} not only enhances the total UC intensity but also alters the electron density population at the up-converting energy levels. The alternation of electron density population at $^2H_{11/2}$, $^4S_{3/2}$ and $^4F_{9/2}$ levels might be ascribed to the change of the non-radiation relaxation probability of the Er^{3+} induced by the doped Nb^{5+} ions. To better understand the related mechanism, the 0.001Er^{3+} mono-doped
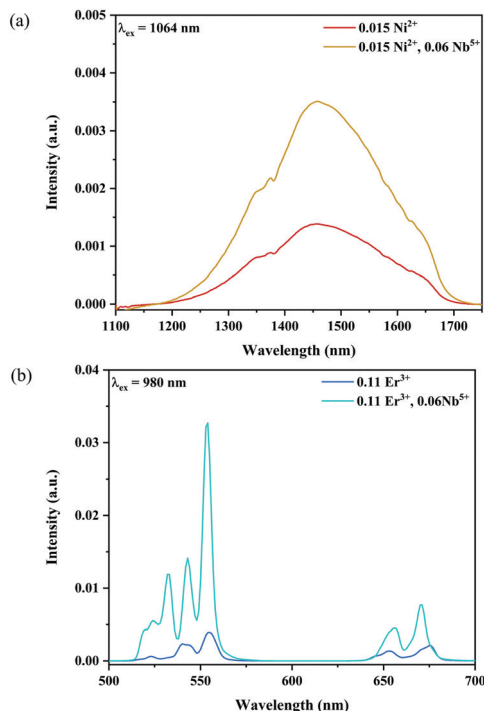
Fig. 7 NIR emission spectra of the Ni^{2+} mono-doped and Ni^{2+}, Nb^{5+} double-doped samples excited at 1064 nm (a), and UC emission spectra of the Er^{3+} mono-doped and Er^{3+}, Nb^{5+} double-doped samples excited at 980 nm (b).

and 0.001Er^{3+}, 0.06Nb^{5+} double-doped samples have been prepared and their emission spectra under 380 nm excitation have also been measured. The percentage of the emission intensity of the $^2H_{11/2} \rightarrow {}^4I_{15/2}$, $^4S_{3/2} \rightarrow {}^4I_{15/2}$ and $^4F_{9/2} \rightarrow {}^4I_{15/2}$ emissions in the total emission intensity for the 0.001Er^{3+} mono-doped and 0.001Er^{3+}, 0.06Nb^{5+} double-doped samples with the excitation at 380 nm is shown in Fig. 8b. A similar phenomenon has also been observed in the low Er^{3+} concentration (0.001) doped case under 380 nm excitation. For the sample doped with low Er^{3+} concentration, the interaction between Er^{3+} ions can be ignored, which is helpful to analyse the process of electron density population at different levels and the non-radiation relaxation properties of Er^{3+}. According to the luminescence mechanism given in Fig. 8c, the following rate equations can be constructed for the low Er^{3+} concentration doped sample under 380 nm excitation:

$$\frac{dn_6}{dt} = -W_{65}n_6 - (A_{61} + A_{62} + A_{63} + A_{64} + A_{65})n_6 + Pn_1 \quad (1)$$

$$\frac{dn_5}{dt} = W_{65}n_6 - (A_{51} + A_{52} + A_{53} + A_{54})n_5 - W_{54}n_5 \quad (2)$$

$$\frac{dn_4}{dt} = W_{54}n_5 - (A_{41} + A_{42} + A_{43})n_4 - W_{43}n_4 \quad (3)$$

$$\frac{dn_3}{dt} = W_{43}n_4 - (A_{31} + A_{32})n_3 - W_{32}n_3 \quad (4)$$

where n_i represents the density of electrons at the corresponding energy level. A_{ij} and W_{ij} are the probabilities of radiative transition
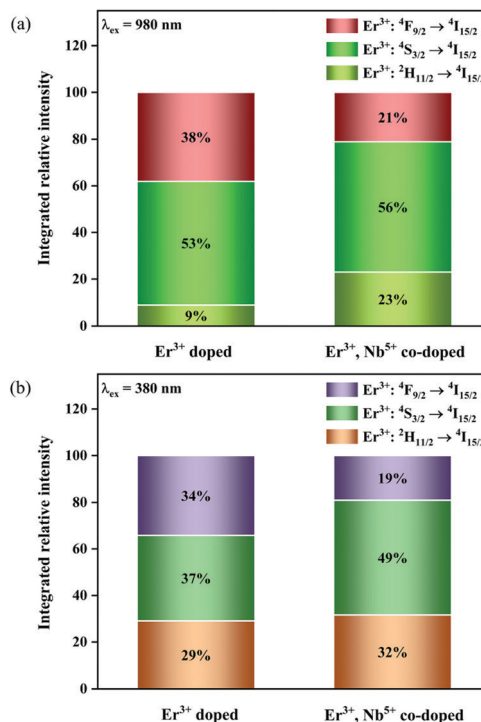

Fig. 8 Percentage of the UC intensity of the $^2H_{11/2} \rightarrow {}^4I_{15/2}$, $^4S_{3/2} \rightarrow {}^4I_{15/2}$ and $^4F_{9/2} \rightarrow {}^4I_{15/2}$ emissions in the total UC emission intensity for the 0.11Er^{3+} mono-doped and 0.11Er^{3+}, 0.06Nb^{5+} double-doped samples under 980 nm excitation (a), percentage of the emission intensity of the $^2H_{11/2} \rightarrow {}^4I_{15/2}$, $^4S_{3/2} \rightarrow {}^4I_{15/2}$ and $^4F_{9/2} \rightarrow {}^4I_{15/2}$ emissions in the total emission intensity for the 0.001Er^{3+} mono-doped and 0.001Er^{3+}, 0.06Nb^{5+} double-doped samples under 380 nm excitation (b) and simplified diagram of the energy transition of Er^{3+} under 380 nm excitation (c).
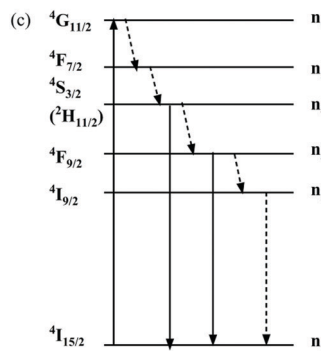
and nonradiative transition from the energy level i to j, respectively. P is the pumping rate from $^4I_{15/2}$ to $^4G_{11/2}$. In the steady state, $dn_i/dt = 0$. According to eqn (1)–(4), an equation can be obtained as:

$$\frac{n_4}{n_3} = \frac{A_{32} + A_{31} + W_{32}}{W_{43}} \quad (5)$$

For the weakly coupled system such as rare earth ions, the nonradiative transition probability can be expressed as:

$$W_{nr}(T) = W_0 \left(1 + n_{av}\right)^p \quad (6)$$

where W_0 is associated with the matrix environment and the electron-phonon coupling strength, and $\left(1 + n_{av}\right)^{p_{ij}}$ is the

temperature-dependent phonon number averaging factor.[44] $n_{av} = (\exp(h\nu/kT) - 1)^{-1}$, which can be regarded as a constant at room temperature (T = 300 K). $p_{ij} = \Delta E_{ij}/h\nu$, where ΔE_{ij} is the energy level gap between the energy level i and j. Therefore, the W_{nr} from the energy level i to j is only related to W_0, and the W_{nr} is positively correlated with the W_0. Combing equation 6 with equation 5, n_4/n_3 can be obtained as:

$$\frac{n_4}{n_3} = \frac{A_{32} + A_{31}}{W_0(1 + n_{av})^{p_{43}}} + (1 + n_{av})^{p_{32}-p_{43}} \quad (7)$$

The emission intensity I_i for the energy level i can be expressed as:

$$I_i = n_i h\nu_i A_i \quad (8)$$

where h is the Planck constant, and ν_i is the radiative transition frequency at the energy level i.[45] Therefore, the intensity relationship between the green light ($^4S_{3/2} \to {}^4I_{15/2}$) and red light ($^4F_{9/2} \to {}^4I_{15/2}$) of Er^{3+} can be expressed as:

$$\frac{I_4}{I_3} \propto \frac{A_{32} + A_{31}}{W_0(1 + n_{av})^{p_{43}}} + (1 + n_{av})^{p_{32}-p_{43}} \quad (9)$$

Of note, a relationship between the nonradiative transition probability factor W' and radiative transition probability A can be constructed as follows:

$$W' \approx 40\frac{c^3}{M_I \Delta E}A \quad (10)$$

where M_I is regarded as the mass of the atom adjacent to the luminous centre. This implies that A is positively correlated with W_{nr}.[46-48] This relationship between the probability of nonradiative transition (W_{nr}) and radiative transition (A) is known as the parallelism relationship. From Fig. 8b, it can be calculated that the intensity ratio between the green ($^4S_{3/2} \to {}^4I_{15/2}$) and red ($^4F_{9/2} \to {}^4I_{15/2}$) emission of the Er^{3+} is 1.39 and 2.67 for the $0.001Er^{3+}$ mono-doped and $0.001Er^{3+}$, $0.06Nb^{5+}$ double-doped samples, respectively. This means that with the introduction of Nb^{5+} ions, the intensity ratio between the green ($^4S_{3/2} \to {}^4I_{15/2}$) and red ($^4F_{9/2} \to {}^4I_{15/2}$) emission, i.e., I_4/I_3 increases. According to the parallelism relationship, the radiative transition probability ($A_{32} + A_{31}$) and nonradiative transition probability (W_{nr}) should simultaneously increase or decrease. When both the radiative transition probability and nonradiative transition probability increase simultaneously and the increase in the radiative transition probability is greater than that of the nonradiative transition probability, the I_4/I_3 will increase. On the contrary, when the radiative transition probability and nonradiative transition probability decrease at the same time and the degree of reduction of the radiative transition probability is less than that of the nonradiative transition probability, the I_4/I_3 will also increase.

In order to confirm the reason for the increase of I_4/I_3, therefore, the fluorescence lifetimes of green light ($^4S_{3/2} \to {}^4I_{15/2}$) for the $0.001Er^{3+}$ mono-doped and $0.001Er^{3+}$, $0.06Nb^{5+}$ double-doped samples are monitored under 380 nm excitation. In the case of low activation ion concentration, the fluorescence lifetime τ can generally be described by the radiative transition

probability A and nonradiative transition probability W_{nr} as follows:[44]

$$\tau = \frac{1}{A + W_{nr}} \quad (11)$$

Fig. 9a shows the luminescence decay curves at 555 nm of the Er^{3+} for the $0.001Er^{3+}$ mono-doped and $0.001Er^{3+}$, $0.06Nb^{5+}$ double-doped samples with 380 nm excitation, respectively. The luminescence decay curves can be well fitted by the double exponential function:

$$I(t) = a_0 + a_1\exp(-t/\tau_1) + a_2\exp(-t/\tau_2) \quad (12)$$

where $I(t)$ denotes the luminescent intensity at time t. a_0, a_1 and a_2 are constants, with τ_1 and τ_2 representing the lifetimes of the exponential components.[49] Their corresponding average lifetimes can be given by the equation:

$$\tau_{av} = \frac{a_1\tau_1^2 + a_2\tau_2^2}{a_1\tau_1 + a_2\tau_2} \quad (13)$$

The calculated fluorescence lifetimes for the $0.001Er^{3+}$ mono-doped and $0.001Er^{3+}$, $0.06Nb^{5+}$ double-doped samples are 0.023 ms and 0.032 ms, respectively, meaning that the doped Nb^{5+} can prolong the fluorescence lifetime of Er^{3+}. According to the parallelism relationship and eqn (11), the prolongation of the fluorescence lifetime means the decrease of radiative transition probability and nonradiative transition probability. Therefore, the increase of I_4/I_3 in the Er^{3+}, Nb^{5+} double-doped phosphor suggests that the doped Nb^{5+} ions reduce both the radiative transition and nonradiative transition probabilities, but the reduction in nonradiative transition probability is larger than that of the radiative transition probability. In addition, the introduction of Nb^{5+} also leads to the enhancement in the emission intensity of Er^{3+} in the $0.001Er^{3+}$, $0.06Nb^{5+}$ double-doped $Y_2Mg_3Ge_3O_{12}$ under excitation of 380 nm. As shown in Fig. 9b, the green emission of the Er^{3+}, Nb^{5+} double-doped sample is increased by 147.7% as compared with that of the Nb^{5+} free one. This indicates that the greatly reduced nonradiative transition probability effectively improves the fluorescence efficiency of the sample.

In addition, the luminescence decay curves at 1450 nm of the Ni^{2+} for the $0.001Ni^{2+}$ mono-doped and $0.001Ni^{2+}$, $0.06Nb^{5+}$ double-doped samples under 455 nm excitation are also measured, as shown in Fig. 9c. The calculated fluorescence lifetimes for the $0.001Ni^{2+}$ mono-doped and $0.001Ni^{2+}$, $0.06Nb^{5+}$ double-doped samples are 0.277 ms and 0.324 ms, respectively. It can be found that the introduction of Nb^{5+} also results in the enhancement of the fluorescence lifetime of the Ni^{2+}. Similarly, with eqn (11) and the parallelism relationship, it can be inferred that the introduction of Nb^{5+} also reduces the radiative transition probability and nonradiative transition probability of the Ni^{2+}. On the other hand, the relative intensity of Ni^{2+}: $^3T_2 \to {}^3A_2$ transition emission for the $0.001Ni^{2+}$ mono-doped and $0.001Ni^{2+}$, $0.06Nb^{5+}$ double-doped samples with the excitation at 455 nm is shown in Fig. 9d. It can be found that the $^3T_2 \to {}^3A_2$ emission intensity of the Ni^{2+} increases by 289.5% with the introduction of Nb^{5+} at 455 nm excitation, meaning that

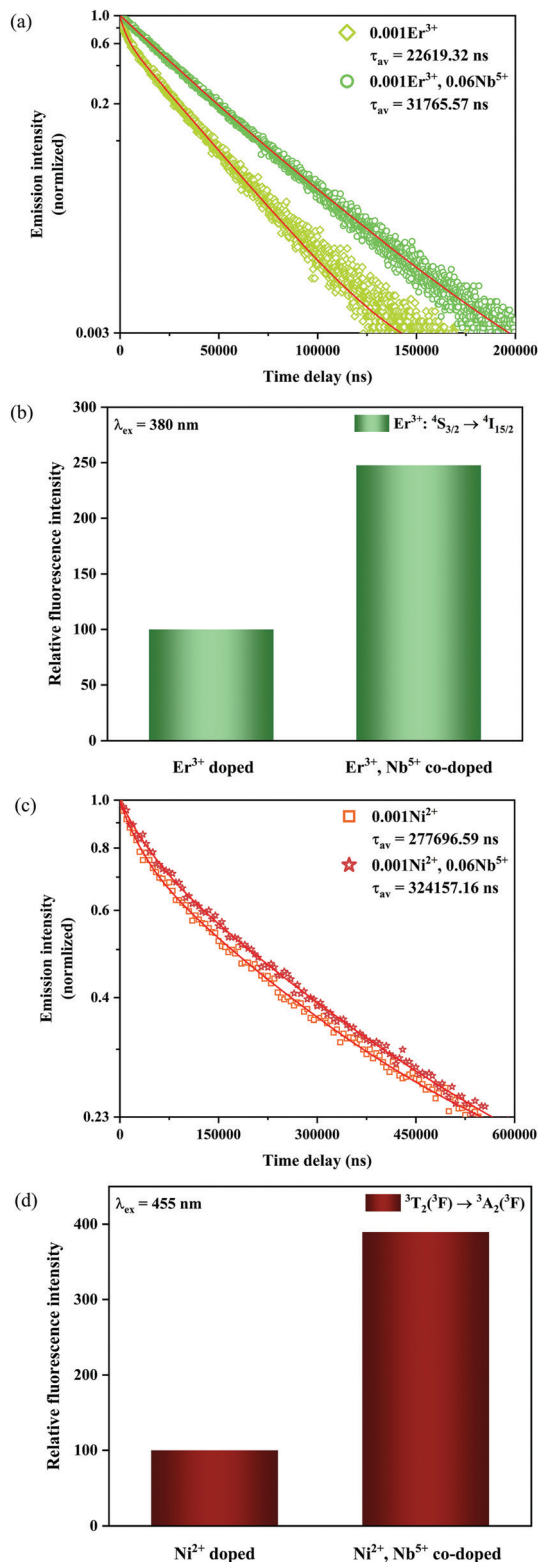decreasing the nonradiative transition probability is also quite helpful for enhancing the Ni^{2+} fluorescence intensity.

In order to explore the effect of the Ni^{2+} and Er^{3+} concentrations on the sensitized UC emission and further optimize the up conversion sample, a series of samples with different Ni^{2+} ion and Er^{3+} ion concentrations have been fabricated. Fig. 10 shows the effect of the Ni^{2+} and Er^{3+} concentrations on the intensity of UC emission under 1064 nm excitation. It can be seen from Fig. 10a that the UC green and red emission intensities increase correspondingly as the Ni^{2+} concentration increases, and reach the maximum at the Ni^{2+} concentration of 0.015 and then decrease with further increasing the Ni^{2+} concentration. The dependence of the UC emission intensity on the concentrations of Er^{3+} is displayed in Fig. 10b. A positive correlation between the Er^{3+} concentrations and the UC green and red emission intensity is shown when the Er^{3+} concentrations do not exceed 0.13. The phosphor gives the strongest UC green and red emission when the Er^{3+} concentration arrives at 0.13. Later on, as the concentration of Er^{3+} increases, the UC emission intensity starts to diminish on account of the energy dissipation from Er^{3+} to Ni^{2+} as well as other nonradiative quenching. Based on the experimental results, the $Y_2Mg_3Ge_3O_{12}:0.015Ni^{2+},0.13Er^{3+},0.06Nb^{5+}$ phosphor manifests the optimal UC emission effectiveness in this work.
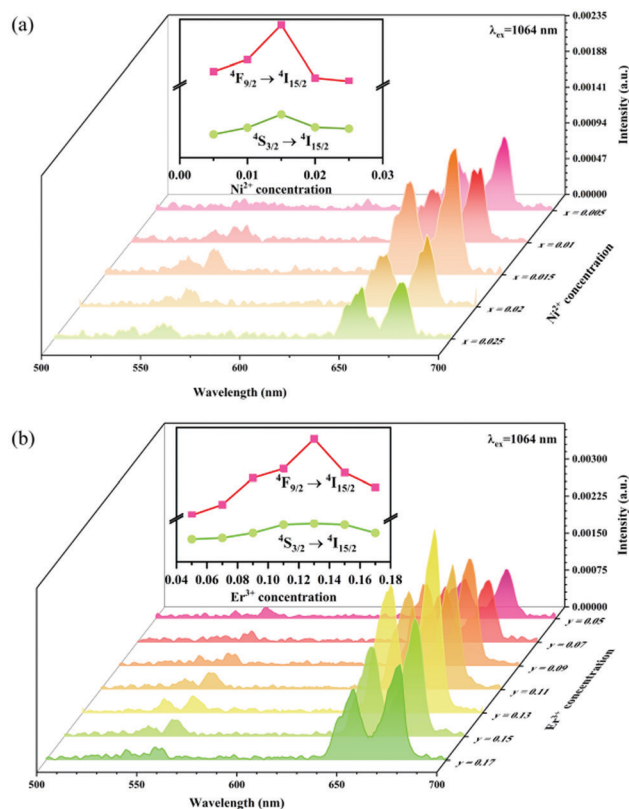
Fig. 9 Fluorescence decay curves (a) as well as relative emission intensity at 555 nm for the $0.001Er^{3+}$ mono-doped and $0.001Er^{3+}$, $0.06Nb^{5+}$ double-doped samples with excitation at 380 nm (b), and fluorescence decay curves (c) as well as relative emission intensity at 1450 nm for the $0.001Ni^{2+}$ mono-doped and $0.001Ni^{2+}$, $0.06Nb^{5+}$ double-doped samples with excitation at 455 nm (d).

Fig. 10 UC emission spectra of $Y_2Mg_3Ge_3O_{12}$: $xNi^{2+},0.11Er^{3+},0.06Nb^{5+}$ (x = 0.005, 0.01, 0.015, 0.02 and 0.025) (a) and $Y_2Mg_3Ge_3O_{12}:0.015$-$Ni^{2+},yEr^{3+},0.06Nb^{5+}$ (y = 0.05, 0.07, 0.09, 0.11, 0.13, 0.15 and 0.17) (b). The insets show the dependence of UC emission intensity on Ni^{2+} and Er^{3+} concentrations, respectively.

It is well known that there is a non-linear dependence between the UC emission intensity I_{em} with the pumping power P, which can usually be described as:

$$I_{em} \propto KP^Q \qquad (14)$$

where K is the material correlation coefficient, and the Q value represents the number of the pump photons required to produce the corresponding UC emission.[50] The UC emission of the $Y_2Mg_3Ge_3O_{12}$:0.015Ni^{2+},0.13Er^{3+},0.06Nb^{5+} sample with different power excitation was measured as shown in Fig. 11. The log-log relationship between the UC emission intensity and the pump power density is also given in the insets of Fig. 11. Fig. 11a records the UC spectra under different 980 nm pumping power variations, and the UC emission intensity shows a positive correlation with the pumping power. The inset in Fig. 11a shows that the UC green and red emission intensity varies as the 980 nm pumping power density increases, respectively. The Q value is 1.97 and 1.99 for the green and red emissions, respectively. This indicates that both the green and red UC emissions of the sample under 980 nm excitation belong to two-photon processes. Fig. 11b records the UC emission spectra under 1064 nm excitation light of different power. The inset in Fig. 11b shows the dependence of the UC green and red emission intensity upon the 1064 nm pumping power density.
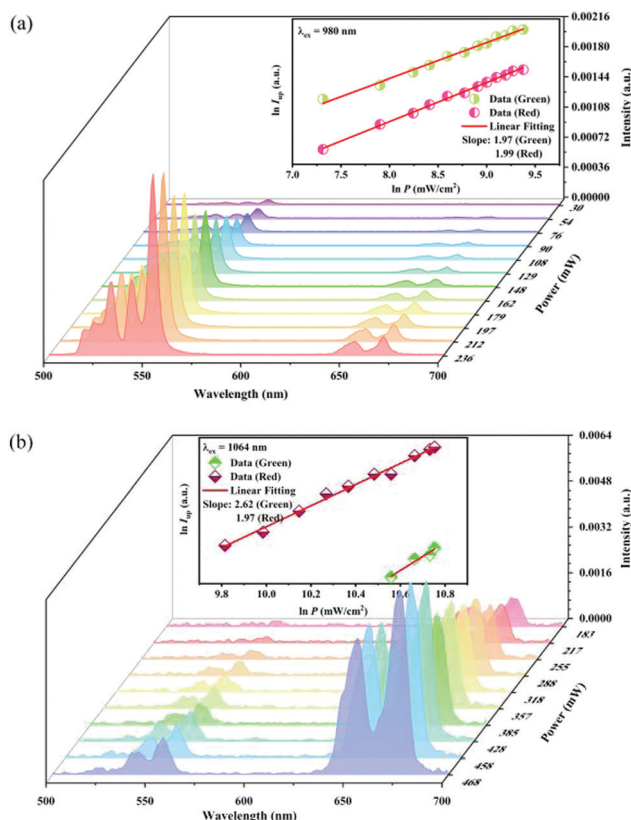

Fig. 11 UC emission intensity of the $Y_2Mg_3Ge_3O_{12}$:0.015-Ni^{2+},0.13Er^{3+},0.06Nb^{5+} sample under the different powers of 980 nm (a) and 1064 nm (b) excitation. The insets show the double logarithmic plots of the excitation power density and the UC emission intensity.

Unlike that under 980 nm excitation, the Q value is 2.62 and 1.97 for the green and red emission, respectively. This means that the red UC emission under 1064 nm excitation is still a two-photon process, while the green UC emission belongs to a three-photon one.

The UC mechanism as well as the energy transfer process is illustrated in Fig. 12. Under excitation of 980 nm, the Er^{3+} ions are raised to the $^4I_{11/2}$ state, and the following $^4I_{11/2}$ (Er^{3+}) + $^4I_{11/2}$ (Er^{3+}) → $^4I_{15/2}$ (Er^{3+}) + $^2H_{11/2}$ (Er^{3+}) energy transfer or the $^4I_{11/2}$ → $^2H_{11/2}$ excited absorption occurs between the Er^{3+} ions, resulting in the population of the $^2H_{11/2}$ state. Then the $^4S_{3/2}$ and $^4F_{9/2}$ are populated due to the nonradiative relaxation process. The $^2H_{11/2}$ → $^4I_{15/2}$, $^4S_{3/2}$ → $^4I_{15/2}$ and $^4F_{9/2}$ → $^4I_{15/2}$ radiative transitions generate the 532 nm, 555 nm and 675 nm emissions. It is evident that both the green emission and red emission are performed by the two-photon process under 980 nm excitation. In the Ni^{2+}, Er^{3+} double-doped sample, however, intense back energy transfer from Er^{3+} to Ni^{2+} might occur under 980 nm excitation, which largely reduces the UC emission of Er^{3+}. Therefore, the UC intensity of the Ni^{2+}, Er^{3+} double-doped sample is much weaker than that of the Er^{3+} mono-doped sample. As shown in Fig. 5a, the UC integral intensities of green emission and red emission for the Ni^{2+}, Er^{3+} double-doped sample weakens by 92% and 97% as compared with that for the Er^{3+} mono-doped sample, respectively.

Since 1064 nm excitation light is located in the absorption band of the Ni^{2+} ion, but not in that of the Er^{3+} ion, the energy transfer from Ni^{2+} to Er^{3+} is responsible for the UC under 1064 nm excitation. In order to understand the energy transfer from Ni^{2+} to Er^{3+} in $Y_2Mg_3Ge_3O_{12}$, the normalized absorption spectra of $Y_2Mg_3Ge_3O_{12}$:Er^{3+} and the normalized emission spectra of $Y_2Mg_3Ge_3O_{12}$:Ni^{2+} excited at 1064 nm are both given in Fig. 13. It can be found that the Er^{3+}: $^4I_{15/2}$ → $^4I_{13/2}$ absorption band is almost completely within the Ni^{2+}: $^3T_2$ → $^3A_2$ emission band. This indicates that the resonant energy transfer from Ni^{2+} to Er^{3+} is allowed in the Ni^{2+}, Er^{3+} double-doped $Y_2Mg_3Ge_3O_{12}$ phosphor. Under 1064 nm excitation, the Ni^{2+} ions in the ground state reach the $^3T_2$ state by absorption of 1064 nm photons, and subsequently the Er^{3+} ions in the nearby ground state are populated to their intermediate state
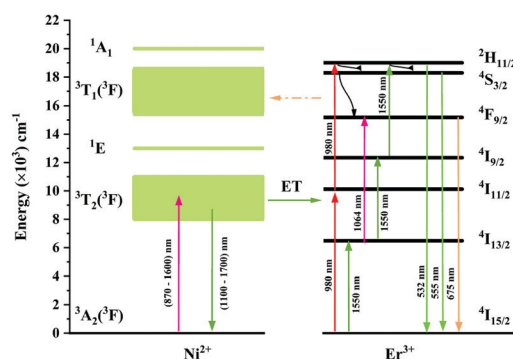

Fig. 12 Energy level schemes of the Ni^{2+} ions and Er^{3+} ions in $Y_2Mg_3Ge_3O_{12}$ and possible energy transfer mechanisms between the Ni^{2+} and Er^{3+} with 980 nm and 1064 nm excitation.

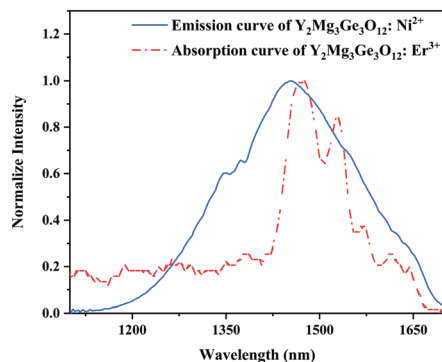**Fig. 13** Normalized emission curve of $Y_2Mg_3Ge_3O_{12}$:Ni^{2+} and absorption curve of $Y_2Mg_3Ge_3O_{12}$:Er^{3+}.

$^4I_{13/2}$ by the $^3T_2$ (Ni^{2+}) + $^4I_{15/2}$ (Er^{3+}) → $^3A_2$ (Ni^{2+}) + $^4I_{13/2}$ (Er^{3+}) energy transfer process. The Er^{3+} ions in the $^4I_{13/2}$ state can be followed by two types of photon transfer processes. In one of them, the Er^{3+} ions in the $^4I_{13/2}$ state allow further absorption of 1064 nm photons to make themselves reach the $^4F_{9/2}$ state, resulting in the red emission at 675 nm. Obviously, this is a two-photon process. In the other one, the Er^{3+} ions are raised to the $^4I_{9/2}$ state by the $^3T_2$ (Ni^{2+}) + $^4I_{13/2}$ (Er^{3+}) → $^3A_2$ (Ni^{2+}) + $^4I_{9/2}$ (Er^{3+}) energy transfer process. The immediately followed energy transfer process $^3T_2$ (Ni^{2+}) + $^4I_{9/2}$ (Er^{3+}) → $^3A_2$ (Ni^{2+}) + $^2H_{11/2}$ (Er^{3+}) causes the Er^{3+} ions in the $^4I_{9/2}$ state to reach their $^2H_{11/2}$ state and the subsequent successive nonradiative relaxation process populates the $^4S_{3/2}$ state of Er^{3+} ions, resulting in the green emission originating in the $^2H_{11/2}$, $^4S_{3/2}$ → $^4I_{15/2}$. Therefore, the green UC emission is a three-photon process.

In order to estimate the energy transfer efficiency and energy transfer rate from Ni^{2+} to Er^{3+}, the time-resolved measurements of the Ni^{2+} emission are performed. Fig. 14a shows the luminescence decay curves of Ni^{2+} emission at 1400 nm for $Y_2Mg_3Ge_3O_{12}$:$0.015Ni^{2+}$,yEr^{3+},$0.06Nb^{5+}$ (y = 0, 0.05, 0.07, 0.09, 0.11 and 0.13) samples with 1064 nm excitation. The Ni^{2+} emission decays more rapidly when the Er^{3+} ions are introduced, which indicates that a nonradiative energy transfer from Ni^{2+} to Er^{3+} takes place. The decay curves can be well fitted by the double exponential function of eqn (12). The average lifetimes can also be calculated by eqn (13). The energy transfer efficiency $\eta_{Ni \to Er}$ and energy transfer rate $\gamma_{Ni \to Er}$ from the Ni^{2+} to the Er^{3+} can be determined by the following equations:[44,51]

$$\eta_{Ni \to Er} = 1 - \frac{\tau}{\tau_0} \qquad (15)$$

$$\gamma_{Ni \to Er} = \frac{1}{\tau} - \frac{1}{\tau_0} \qquad (16)$$

where τ_0 and τ are the lifetime of Ni^{2+} at y = 0 and $y \neq 0$, respectively. Fig. 14b shows the variation of the fluorescence lifetime of Ni^{2+}, the energy transfer efficiency $\eta_{Ni \to Er}$ as well as the energy transfer rate $\gamma_{Ni \to Er}$ with the doping concentration of Er^{3+} ions. As the concentration of Er^{3+} ions increases, $\eta_{Ni \to Er}$ and $\gamma_{Ni \to Er}$ also increase. The energy transfer efficiency is as
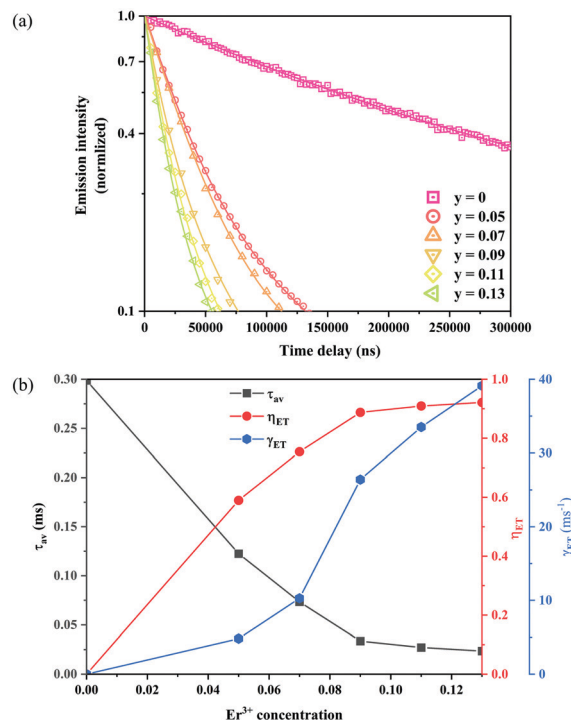
Fig. 14 Fluorescence decay curves at 1400 nm for Ni^{2+} emission under 1064 nm excitation of $Y_2Mg_3Ge_3O_{12}$:$0.015Ni^{2+}$,yEr^{3+},$0.06Nb^{5+}$ (y = 0, 0.05, 0.07, 0.09, 0.11 and 0.13) samples (a); the variations of fluorescence lifetime τ of Ni^{2+}, as well as energy transfer efficiency $\eta_{Ni \to Er}$ and energy transfer rate $\gamma_{Ni \to Er}$ from Ni^{2+} to Er^{3+} with the Er^{3+} ion doping concentration (b).

high as 92.1% and the energy transfer rate is 39.1 ms^{-1} at y = 0.13, at which the sample shows the strongest UC.

To better know the $Ni^{2+} \to Er^{3+}$ energy transfer process, the NIR emission spectra of $Y_2Mg_3Ge_3O_{12}$:$0.015Ni^{2+}$,yEr^{3+},$0.06Nb^{5+}$ phosphors under 1064 nm excitation are also measured, as shown in Fig. 15a. Since the Er^{3+} cannot be excited by 1064 nm directly, the presence of NIR emission peaking at 1536 nm due to the $^4I_{13/2} \to {}^4I_{15/2}$ transition of Er^{3+} in Fig. 15a should be ascribed to the $Ni^{2+} \to Er^{3+}$ energy transfer. Moreover, it is also found that the NIR emission of Ni^{2+} drastically weakens with the increase of the concentration of the doped Er^{3+}. The NIR emission properties of the Ni^{2+}, Er^{3+} double-doped phosphors under 1064 nm excitation further prove the occurrence of the efficient $Ni^{2+} \to Er^{3+}$ energy transfer. In general, the energy transfer mechanisms include exchange interaction and electrical multipolar interaction. These two mechanisms can be distinguished by the critical distance (R_C). In theory, when the value of R_C is less than 5 Å, the exchange interaction is predominant. On the contrary, the electric multipole interaction will predominate when the value of R_C is above 5 Å. R_C can be calculated according to the following equation given by Blasse:

$$R_C = 2\left(\frac{3V}{4\pi\chi N}\right)^{1/3} \qquad (17)$$

where V is the volume of the unit cell; χ represents the total concentration of Ni^{2+} and Er^{3+} when Er^{3+} emission intensity begins
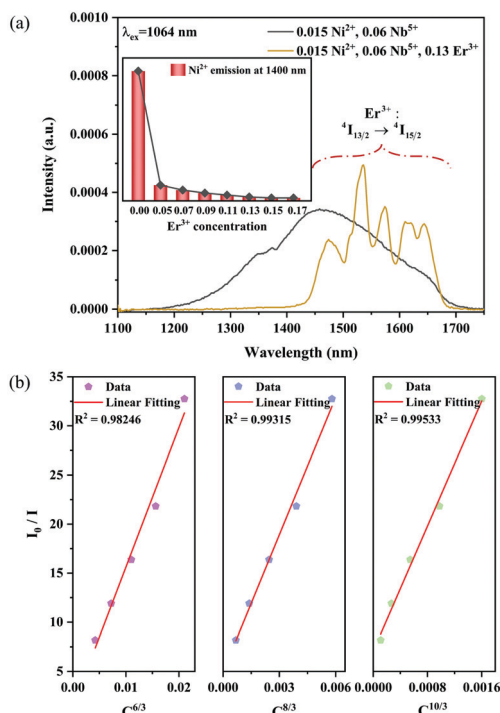
Fig. 15 NIR emission spectra of the $0.015Ni^{2+},0.06Nb^{5+}$ double-doped and $0.015Ni^{2+},0.13Er^{3+},0.06Nb^{5+}$ tri-doped samples under 1064 nm excitation (a); the dependence of I_0/I on $C^{6/3}$, $C^{8/3}$ and $C^{10/3}$ (b). The inset shows the dependence of the emission intensity of Ni^{2+} at 1400 nm on the Er^{3+} concentrations.

to weaken; N is the number of available sites of dopant in each unit cell.[52] And here $V = 1837.77$ Å^3, $\chi = 0.145$ and $N = 8$. The calculated value of R_C is about 14.464 Å and is above 5 Å. Thus, the energy transfer mechanism is dominated by the electric multipolar interaction for the $Y_2Mg_3Ge_3O_{12}:Ni^{2+},Er^{3+},Nb^{5+}$ phosphor. The types of electric multipolar interaction can be determined by fitting eqn (18) following the Dexter energy transfer theory:

$$\frac{I_0}{I} \propto C^{n/3} \tag{18}$$

where I_0 denotes the emission intensity of Ni^{2+}: $^3T_2 \rightarrow {}^3A_2$ for the $Y_2Mg_3Ge_3O_{12}:0.015Ni^{2+},0.06Nb^{5+}$ phosphor. I is the emission
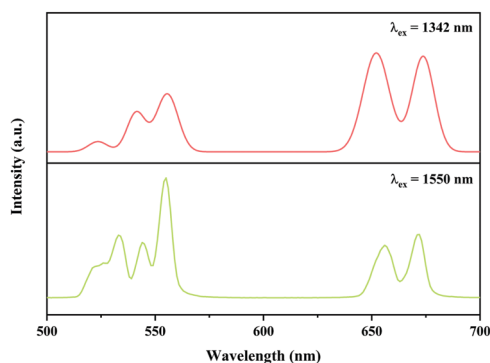
Fig. 16 UC emission spectra of $Y_2Mg_3Ge_3O_{12}:0.015Ni^{2+}$, $0.13Er^{3+}$, $0.06Nb^{5+}$ phosphor with excitation at 1342 nm and 1550 nm.

Table 2 Comparison of broadband sensitized Ni^{2+}, Er^{3+} double-doped UC materials

Host	Excitation (nm)	Emission (nm)	$\eta_{Ni \rightarrow Er}$	Ref
$CaTiO_3$	1200	980	0.97	31
$SrZrO_3$	1200	980	0.98	32
$LaScO_3$	1180	980	0.99	33
$Gd_3Ga_5O_{12}$	1180	980	0.98	34
$Ca_3Ga_2Ge_3O_{12}$	1180	980	0.96	35
$MgGa_2O_4$	1064	660	0.11	36
$Y_2Mg_3Ge_3O_{12}$	1064	532/555/675	0.92	This work

intensity of Ni^{2+}: $^3T_2 \rightarrow {}^3A_2$ for the $Y_2Mg_3Ge_3O_{12}:0.015$-$Ni^{2+}yEr^{3+},0.06Nb^{5+}$ phosphors. C is the total doping concentration of Ni^{2+} ions and Er^{3+} ions. n is a constant and the number of n can be 6, 8 and 10, which corresponds to dipole–dipole, dipole–quadrupole and quadrupole–quadrupole interactions, respectively. The dependence of I_0/I on $C^{n/3}$ is shown in Fig. 15b. The linear relationship displays the best fitting when $n = 10$. The results indicate that the energy transfer from Ni^{2+} to Er^{3+} in $Y_2Mg_3Ge_3O_{12}:$-Ni^{2+},Er^{3+},Nb^{5+} phosphors is a quadrupole–quadrupole interaction.

In addition, the Ni^{2+}, Er^{3+} double-doped $Y_2Mg_3Ge_3O_{12}$ phosphor might have the potential to convert light within the broadband range of 900–1700 nm into visible emission, considering the broad absorption band (900–1700 nm) of the Ni^{2+} and Er^{3+} ions in the $Y_2Mg_3Ge_3O_{12}$ matrix and the $Ni^{2+} \rightarrow Er^{3+}$ energy transfer pathway therein. To verify its broadband UC performance, the UC emission of the $Y_2Mg_3Ge_3O_{12}:0.015Ni^{2+},0.13Er^{3+},0.06Nb^{5+}$ phosphor with the excitation of 1342 nm and 1550 nm are also measured. Similar to that with 1064 nm and 980 nm excitation, the UC emissions at 532 nm, 555 nm and 675 nm due to the $^2H_{11/2} \rightarrow {}^4I_{15/2}$, $^4S_{3/2} \rightarrow {}^4I_{15/2}$ and $^4F_{9/2} \rightarrow {}^4I_{15/2}$ transitions of the Er^{3+} are also observed under excitation of 1342 nm and 1550 nm, respectively, as shown in Fig. 16. Obviously, the UC emission under 1550 nm excitation is performed by successive energy transfer between Er^{3+} as well as Er^{3+} excited state absorption since Er^{3+} can be directly excited by 1550 nm light, while the UC emission under 1342 nm is realized by the $Ni^{2+} \rightarrow Er^{3+}$ energy transfer because the 1342 nm is not within the absorption band of Er^{3+}, but within the absorption band of Ni^{2+}. It is worth noting that the $Y_2Mg_3Ge_3O_{12}:Ni^{2+},Er^{3+},Nb^{5+}$ phosphor in this work gives strong visible UC emission at 532 nm, 555 nm and 675nm under excitation of light in a wide near infrared range, unlike the previously reported broadband sensitized Ni^{2+}, Er^{3+} double-doped UC materials that gave near infrared UC emission at 980 nm. Table 2 shows the comparison of UC performance between some reported Ni^{2+}, Er^{3+} double-doped materials and the $Y_2Mg_3Ge_3O_{12}:Ni^{2+},Er^{3+},Nb^{5+}$ phosphor in the present work. It can be found that the energy transfer efficiency from Ni^{2+} to Er^{3+} in the $Y_2Mg_3Ge_3O_{12}:Ni^{2+},Er^{3+},Nb^{5+}$ phosphor is similar to that reported in previous literature. The broadband sensitized visible UC performance of the $Y_2Mg_3Ge_3O_{12}:Ni^{2+},Er^{3+},Nb^{5+}$ phosphor might open up new applications in the photoelectron field.

4. Conclusions

In this work, Ni^{2+}, Er^{3+} and Nb^{5+} tri-doped $Y_2Mg_3Ge_3O_{12}$ phosphors have been synthesized by a conventional solid-

phase reaction method. The UC emissions at 532 nm, 555 nm and 675 nm have been observed under excitation of 980 nm, 1064 nm, 1342 nm and 1550 nm, respectively. It was found that the $Ni^{2+} \rightarrow Er^{3+}$ energy transfer, Er^{3+}-Er^{3+} interaction as well as Er^{3+} excited state absorption provide abundant channels for the UC process, making it capable of converting light within the wide band range of 900–1700 nm into visible emission. The additional Nb^{5+} ions can reduce both the radiative transition probability and nonradiative transition probability of Ni^{2+} and Er^{3+} ions simultaneously and the decrease of nonradiative transition probability is greater than that of the radiative transition probability, which leads to a more intense UC emission. The optimum UC emission intensity is achieved when the doping concentrations of Ni^{2+}, Er^{3+} and Nb^{5+} are 0.015, 0.13 and 0.06, respectively, of which the efficiency of $Ni^{2+} \rightarrow Er^{3+}$ energy transfer caused by the quadrupole-quadrupole interaction is as high as 92.1%. The newly developed UC material in the present work has potential application in c-Si solar cells, infrared detectors and other spectral conversion devices.

Conflicts of interest

There are no conflicts to declare.

Acknowledgements

Notes and references

1 H. Scheife, G. Huber, E. Heumann, S. Bär and E. Osiac, *Opt. Mater.*, 2004, **26**, 365–374.
2 S. Wen, J. Zhou, K. Zheng, A. Bednarkiewicz, X. Liu and D. Jin, *Nat. Commun.*, 2018, **9**, 2415.
3 M. Gu, Q. Zhang and S. Lamon, *Nat. Rev. Mater.*, 2016, **1**, 16070.
4 S. Jiang, P. Zeng, L. Liao, S. Tian, H. Guo, Y. Chen, C. Duan and M. Yin, *J. Alloys Compd.*, 2014, **617**, 538–541.
5 M. Zhang, Y. Lin, T. J. Mullen, W.-F. Lin, L.-D. Sun, C.-H. Yan, T. E. Patten, D. Wang and G.-Y. Liu, *J. Phys. Chem. Lett.*, 2012, **3**, 3188–3192.
6 J. Tao, J. Chen, D. Ban, M. G. Helander and Z. H. Lu, *Sci. Adv. Mater.*, 2012, **4**, 266–281.
7 Y. Liu, X. Meng and W. Bu, *Coord. Chem. Rev.*, 2019, **379**, 82–98.
8 M. Alkahtani, Y. Chen, J. J. Pedraza, J. M. González, D. Y. Parkinson, P. R. Hemmer and H. Liang, *Opt. Express*, 2017, **25**, 1030–1039.
9 K.-Q. Peng and S.-T. Lee, *Adv. Mater.*, 2011, **23**, 198–215.
10 Y. Liang, Y. Wu, D. Feng, S.-T. Tsai, H.-J. Son, G. Li and L. Yu, *J. Am. Chem. Soc.*, 2009, **131**, 56–57.
11 W. Shockley and H. J. Queisser, *J. Appl. Phys.*, 1961, **32**, 510–519.
12 X. Huang, *J. Alloys Compd.*, 2017, **690**, 356–359.
13 J. C. Goldschmidt and S. Fischer, *Adv. Opt. Mater.*, 2015, **3**, 510–535.
14 L. C. Hirst and N. J. Ekins-Daukes, *Prog. Photovoltaics Res. Appl.*, 2011, **19**, 286–293.
15 T. Trupke, M. A. Green and P. Würfel, *J. Appl. Phys.*, 2002, **92**, 4117–4122.
16 S. Fischer, A. Ivaturi, B. Fröhlich, M. Rüdiger, A. Richter, K. W. Krämer, B. S. Richards and J. C. Goldschmidt, *IEEE J. Photovolt.*, 2014, **4**, 183–189.
17 B. M. van der Ende, L. Aarts and A. Meijerink, *Phys. Chem. Chem. Phys.*, 2009, **11**, 11081–11095.
18 M. Kaiser, C. Würth, M. Kraft, I. Hyppänen, T. Soukka and U. Resch-Genger, *Nanoscale*, 2017, **9**, 10051–10058.
19 E. I. Madirov, V. A. Konyushkin, A. N. Nakladov, P. P. Fedorov, T. Bergfeldt, D. Busko, I. A. Howard, B. S. Richards, S. V. Kuznetsov and A. Turshatov, *J. Mater. Chem. C*, 2021, **9**, 3493–3503.
20 M. Pokhrel, G. A. Kumar and D. K. Sardar, *J. Mater. Chem. A*, 2013, **1**, 11595–11606.
21 I. Etchart, A. Huignard, M. Bérard, M. N. Nordin, I. Hernández, R. J. Curry, W. P. Gillin and A. K. Cheetham, *J. Mater. Chem.*, 2010, **20**, 3989–3994.
22 S. Heer, K. Kömpe, H.-U. Güdel and M. Haase, *Adv. Mater.*, 2004, **16**, 2102–2105.
23 F. Wang and X. Liu, *J. Am. Chem. Soc.*, 2008, **130**, 5642–5643.
24 F. Vetrone, J.-C. Boyer, J. A. Capobianco, A. Speghini and M. Bettinelli, *J. Appl. Phys.*, 2004, **96**, 661–667.
25 X. Xie and X. Liu, *Nat. Mater.*, 2012, **11**, 842–843.
26 W. Yan, F. Liu, Y.-Y. Lu, X.-J. Wang, M. Yin and Z. Pan, *Opt. Express*, 2010, **18**, 20215–20221.
27 M. G. Brik, C. N. Avram and N. M. Avram, *J. Phys. Chem. Solids*, 2008, **69**, 1796–1801.
28 W. E. Vehse, K. H. Lee, S. I. Yun and W. A. Sibley, *J. Lumin.*, 1975, **10**, 149–162.
29 S. Ye, E. H. Song, E. Ma, S. J. Zhang, J. Wang, X. Y. Chen, Q. Y. Zhang and J. R. Qiu, *Opt. Mater. Express*, 2014, **4**, 638–648.
30 P. Gerner, K. Krämer and H. U. Güdel, *J. Lumin.*, 2003, **102-103**, 112–118.
31 H. N. Luitel, S. Mizuno, T. Tani and Y. Takeda, *J. Ceram. Soc. Jpn.*, 2017, **125**, 821–828.
32 H. N. Luitel, S. Mizuno, T. Tani and Y. Takeda, *Opt.Mater.*, 2017, **64**, 314–322.
33 Y. Takeda, S. Mizuno, H. N. Luitel, K.-I. Yamanaka and T. Tani, *J. Appl. Phys.*, 2016, **120**, 073102.
34 Y. Takeda, H. N. Luitel and S. Mizuno, *Jpn. J. Appl. Phys.*, 2018, **57**, 08RF02.
35 Y. Takeda, S. Mizuno, H. N. Luitel and T. Tani, *J. Am. Ceram. Soc.*, 2019, **102**, 3457–3467.
36 X. Zou, S. Xiao and X. Yang, *Ceram. Int.*, 2021, **47**, 13853–13858.
37 W. Guan, S. Xiao and X. Yang, *J. Lumin.*, 2020, **217**, 116795.
38 H. Lin, J. Xu, Q. Huang, B. Wang, H. Chen, Z. Lin and Y. Wang, *ACS Appl. Mater. Interfaces*, 2015, **7**, 21835–21843.
39 C. Ji, Z. Huang, X. Tian, H. He, J. Wen and Y. Peng, *J. Alloys Compd.*, 2020, **825**, 154176.

40 J. Niu, Z. Zhang, W. Zhou and H. Du, *J. Mater. Sci.: Mater. Electron.*, 2020, **31**, 4113–4120.

41 T. Jansen, J. Gorobez, M. Kirm, M. G. Brik, S. Vielhauer, M. Oja, N. M. Khaidukov, V. N. Makhov and T. Jüstel, *ECS J. Solid State Sci. Technol.*, 2017, **7**, R3086–R3092.

42 P. Zhang, Y. Wang, M. Lin, D. Zhang, X. Ren and Q. Yuan, *J. Electrochem. Soc.*, 2012, **159**, A402–A409.

43 A. C. Silva, D. Q. L. Oliveira, L. C. A. Oliveira, A. S. Anastácio, T. C. Ramalho, J. H. Lopes, H. W. P. Carvalho and C. E. R. Torres, *Appl. Catal. A*, 2009, **357**, 79–84.

44 R. Reisfeld, *Rare Earths*, Springer, 1975, pp. 123–175.

45 X. Zou and H. Toratani, *J. Non-Cryst. Solids*, 1995, **181**, 87–99.

46 Z.-D. Luo, *Chem. Phys. Lett.*, 1983, **94**, 498–504.

47 D. S. Ray and M. Chowdhury, *Chem. Phys.*, 1981, **61**, 157–169.

48 M. F. H. Schuurmans and J. M. F. van Dijk, *Phys. B + C*, 1984, **123**, 131–155.

49 J. R. Lakowicz, *Principles of Fluorescence Spectroscopy*, Springer, US, 2013.

50 M. Pollnau, D. R. Gamelin, S. R. Lüthi, H. U. Güdel and M. P. Hehlen, *Phys. Rev. B: Condens. Matter Mater. Phys.*, 2000, **61**, 3337–3346.

51 Q. Y. Meng, Z. X. Liu and W. J. Sun, *Acta Phys. Sin.*, 2013, **62**, 097801.

52 Z. Wang, L. Cheng, H. Tang, X. Yu, J. Xie, X. Mi, Q. Liu and X. Zhang, *J. Solid State Chem.*, 2021, **301**, 122295.